In situ x-ray studies of the incipient ZnO atomic layer deposition on $In_{0.53}Ga_{0.47}As$

E. V. Skopin,[1,*] L. Rapenne,[1] J. L. Deschanvres,[1] E. Blanquet,[2] G. Ciatto,[3] L. Pithan,[4] D. D. Fong,[5] M.-I. Richard,[6,7] and H. Renevier[1,†]

[1]*Univ. Grenoble Alpes, CNRS, Grenoble INP‡, LMGP, 38000 Grenoble, France*
[2]*Univ. Grenoble Alpes, CNRS, Grenoble INP‡, SIMAP, 38000 Grenoble, France*
[3]*Synchrotron SOLEIL, Beamline SIRIUS, L'Orme des Merisiers, Saint-Aubin, F-91192 Gif sur Yvette, France*
[4]*European Synchrotron Radiation Facility, ID3, 71 Avenue des Martyrs, 38043 Grenoble, France*
[5]*Materials Science Division, Argonne National Laboratory, 9700 South Cass Avenue, Argonne, Illinois 60439, USA*
[6]*Aix-Marseille Université, CNRS, Université de Toulon, IM2NP UMR 7334, 13397 Marseille, France*
[7]*European Synchrotron Radiation Facility, ID1, 71 Avenue des Martyrs, 38043 Grenoble, France*

(Received 12 October 2019; accepted 20 March 2020; published 27 April 2020)

We describe in detail how ZnO films grow on $In_{0.53}Ga_{0.47}As$ substrates by atomic layer deposition (ALD), employing a suite of *in situ* synchrotron x-ray techniques. Combining results from different measurements allows the distinguishment of three different growth behaviors: an initial, slow linear growth, often referred to as a growth delay (regime I), followed by a nonlinear growth (regime II), and finally, a steady, linear growth (regime III), the last of which is the self-limited growth behavior characteristic of ALD. By the end of regime I, the $In_{0.53}Ga_{0.47}As$ surface is covered with an ultrathin, poorly ordered Zn oxide layer. The transition from regime I to II is clearly evidenced by the appearance in the x-ray absorption spectra of characteristic features of the wurtzite structure, as well as the nucleation and growth of ZnO grains (three-dimensional) on top of the poorly ordered Zn oxide layer. Regime II ends when the growth per cycle reaches a constant level. We show that the water pressure during growth has an impact on the duration of the growth delay (regime I), unlike the substrate temperature. In the regime of steady growth, we observe that the rate of deposition obtained for all temperatures inside the ALD window is 0.17 nm cy^{-1}. The deposition temperature has clear effects on the film texture and initial crystallization behavior, as well as the final crystallinity and thicknesses of the layers adjacent to the $In_{0.53}Ga_{0.47}As$ substrate. Based on the experimental results and earlier *ab initio* calculations and Monte Carlo simulations of ZnO ALD on ZnO, we suggest reaction mechanisms consistent with our findings, and we present a model of growth starting from the very earliest stages of deposition to the steady growth regime.

DOI: 10.1103/PhysRevMaterials.4.043403

I. INTRODUCTION

For the past several years, the rapid and continuous increase in transistor density and switching speeds has led to the consideration of III-V semiconductors as replacements for silicon in metal oxide semiconductor field-effect transistors (MOSFETs) [1,2]. $In_xGa_{1-x}As$ is of particular interest due to its high charge carrier mobility, which is almost a factor of 10 higher than that for Si. By varying the ratio of In to Ga in $In_xGa_{1-x}As$ [3,4], it is possible to choose the $In_xGa_{1-x}As$ lattice parameter (from 0.606 to 0.565 nm) and the direct band-gap value, from 0.354 eV (InAs) to 1.424 eV (GaAs). For this reason, this material is already widely used in infrared (IR) electronics [5]: many IR receivers and emitters, high-power diode lasers, devices for high-current electronics, and microwave electronics are based on $In_{0.53}Ga_{0.47}As$/InP heterostructures (where $x = 0.53$ is chosen to match the InP lattice parameter).

One of the key technological problems in the development of high-performance MOSFETs concerns the quality of the metal-semiconductor contact, which must be Ohmic with a specific contact resistivity less than $\rho_c = 10^{-8}\ \Omega\,cm^2$ [6]. Here, pinning of the metal Fermi level is a major issue as it can lead to the formation of a Schottky barrier for charge carriers [7,8]. One possible solution is forming a metal-insulator-semiconductor structure, i.e., to insert an ultrathin, dielectric oxide between the metal and the $In_xGa_{1-x}As$ semiconductor. However, the oxide must be sufficiently thin (less than 10 nm) to allow flow of the tunneling current [6]. Such oxide layers can also be used as interfacial passivation layers (IPLs) [9–11] grown on $In_xGa_{1-x}As$ under the gate dielectric.

One of the most promising materials for both depinning the metal Fermi level and creation of the IPL is ZnO. It was shown previously that the insertion of an ultrathin ZnO layer between $In_xGa_{1-x}As$ and the Al metal contact decreases the contact resistance [6,12]. Likewise, a ZnO IPL is known to suppress film crystallization and oxide formation, reduce interface state density, and improve the interface quality [10,11].

A highly scalable method for deposition of such a thin oxide layer is thermal atomic layer deposition (ALD) [13]. ALD is based on self-limiting surface chemical reactions, allowing the layer-by-layer growth of ultrathin, dense films with smooth surfaces [14]. The comparatively low substrate temperatures required for ALD make it possible to reduce the

*evgeniy.v.skopin@gmail.com
†hubert.renevier@grenoble-inp.fr
‡Institute of Engineering Univ. Grenoble Alpes.

thermal budget during manufacturing of the transistor. For the ALD of ZnO, the substrate temperature can range from room temperature to a few hundred degrees Celsius [15].

The growth process involves the cyclical injection of time-separated gases into a chamber, within which they react with a heated substrate [16]. One ALD cycle consists of the following: the injection of precursor A and its subsequent reaction with the sample surface, followed by a purge; the injection of precursor B and its subsequent reaction with the sample surface, followed by a purge. In the case of ideal ALD, the thickness of the deposited layer is controlled only by the number of cycles. Since growth relies on chemisorption of the precursor onto the sample surface, the most important parameters for ALD are the substrate temperature, the surface functionalization, and the precursor chemistry. It is therefore expected that the initial growth behavior (ALD on the substrate) may be different from that in subsequent growth stages (ALD on the deposited material). Indeed, the presence of a ZnO transient prior to steady-state growth has been demonstrated on various substrate surfaces. For instance, Fong *et al.* [17] showed that ZnO films deposited on Si grow initially in the form of islands, with the onset of coalescence occurring during the fourth growth cycle. Baji *et al.* [18] showed that the ZnO growth behavior depends strongly on the substrate, exhibiting islandlike growth on Si and layer-by-layer growth on GaN; on sapphire, the growth mode can be tuned by the deposition temperature. Consequently, to create ultrathin ZnO layers using ALD, one needs to know and understand how growth occurs at the initial stages, i.e., how thickness varies with the number of cycles, how the parameters of the process affect growth (e.g., precursor flows, substrate temperature), and how the atomic structure of the deposited material varies with film thickness.

Many *in situ* techniques have been used to investigate the initial stages: mass spectrometry, quartz microbalance, infrared spectrometry, surface photoabsorption, incremental dielectric reflection, surface photon interference, reflectance difference spectroscopy, optical emission spectrometry, and spectroscopic ellipsometry [19,20]. Various synchrotron techniques have also been used to study both the structure and composition of ultrathin films, exploiting the high brilliance of the beam, the possibility of changing the x-ray energy, and the availability of two-dimensional (2D) detectors. X-ray fluorescence (XRF), x-ray diffraction (XRD), specular reflectivity (XRR), x-ray absorption fine structure spectroscopy (XAFS), and grazing incidence small-angle x-ray scattering (GISAXS) are among the popular techniques used for *in situ* growth studies at various synchrotron centers [17,21–23].

Here, we employ *in situ* synchrotron techniques to study the initial growth behavior of ZnO ALD on $In_xGa_{1-x}As$, as well as to characterize the resulting film morphology and crystallinity. We exploit a custom-built thermal ALD reactor [24,25] equipped with a dedicated port for measuring x-ray fluorescence and a rotating flange for performing surface diffraction. In a previous *in situ* x-ray study [26], ZnO growth on (001)$In_xGa_{1-x}As$ substrates by ALD was monitored by Zn $K\alpha$ XRF and XAFS at the Zn K-edge. Here, we explore the ZnO layer crystallization mechanism and mainly focus on the results of in-plane XRD measurements conducted during ZnO ALD in the substrate temperature range of 120-240 °C.

The reactor was installed on the heavy-duty diffractometer of beamline ID3 [27] at ESRF (Grenoble, France). ZnO ALD on $In_{0.53}Ga_{0.47}As$ was monitored *in situ* by measuring Zn $K\alpha$ XRF, XRR, and in-plane reciprocal space maps (RSMs). Several samples were also selected for postgrowth imaging studies by transmission electron microscopy (TEM).

II. EXPERIMENT

The $In_{0.53}Ga_{0.47}As$ (001) substrates (hereafter denoted InGaAs) were provided by G.I.E III-V Lab (Palaiseau, France). More details about the substrate growth can be found in Ref. [26]. Prior to growth, the InGaAs substrates were agitated in 4M HCl solution for 5 min to remove the native oxide, rinsed in deionized water for 30 s, and then dried with argon before immediate introduction into the ALD reactor. The substrates were then annealed at 200 °C for 30 min in the reactor under a constant flow of 100 sccm nitrogen to evaporate As from the surface.

During the ALD process, we used $Zn(C_2H_5)_2$ or diethylzinc (DEZn) as the metal precursor, water (H_2O) as the oxidant, and nitrogen (N_2) as the purge gas. For each ALD cycle, the flow of DEZn was 5 sccm, and the pulse duration was 5 s, while the water flow ranged between 0.6 and 6.0 sccm with a pulse length of 40 s. To clear the reactor between the DEZn and H_2O pulses, N_2 was injected into the chamber, flowing to the pump at a rate of 1000 sccm for 45 s.

XRR and XRF data were recorded with an x-ray energy of 20 and 10 keV (above the Zn K-edge at 9.659 keV), respectively, either during each ALD cycle or after the completion of several ALD cycles (without x-rays) while purging the reactor with 100 sccm flow of nitrogen. For studies of the in-plane crystal structure, the energy was set to 20 keV in order to quickly sample a wide range of reciprocal space. In-plane diffraction measurements were obtained by measuring a series of so-called zap-scans with a 2D Maxipix™ pixel detector. The incident angle was 0.35°, i.e., above the InGaAs and ZnO critical angle values at 20 keV (0.129° and 0.137°, respectively). The resulting set of detector images were analyzed using BINOCULARS [28] data reduction and analysis software to plot the in-plane RSMs.

The TEM observations were carried out at 200 kV with a JEOL 2010 microscope (with a resolution of ∼0.19 nm). Cross-sectioned samples were prepared by both manual and automated polishing, the latter using the MultiPrep™ system (Allied High Tech Products, Inc.). The final polishing was performed using a felt-covered disk impregnated with a silica solution until the appearance of the first extinction fringe among those of equal thickness. Ar-ion milling was then used to minimize the total thickness.

III. RESULTS

A. Substrate temperature and water pressure effects

Figure 1 displays the equivalent film thickness, as determined by the calibrated Zn $K\alpha$ fluorescence signal, as a function of the number of ALD cycles for four substrate temperatures: 120, 160, 200, and 240 °C. We denote the corresponding samples as 120, 160, 200, and 240 below. The three lower temperatures lie within the reported ALD window

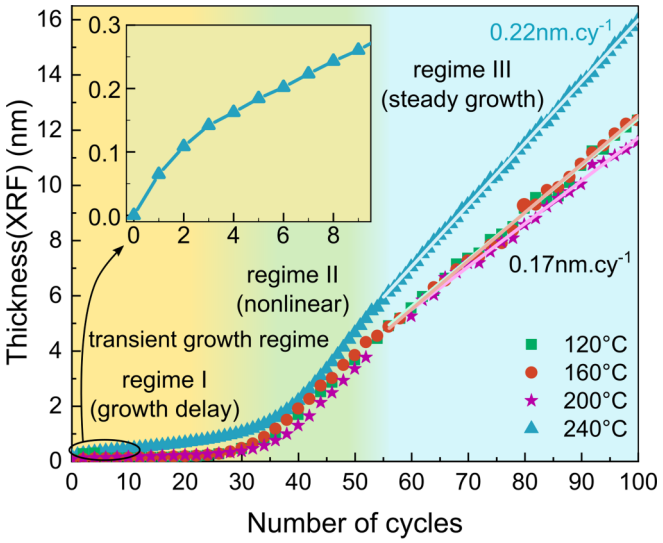

FIG. 1. Equivalent Thickness(XRF) of the deposited ZnO layers as a function of ALD cycle number for four different substrate temperatures: 120 °C (green squares), 160 °C (dark red circles), 200 °C (purple stars), and 240 °C (light blue triangles). Inset: Close-up of the Thickness(XRF) vs cycle number for the 240 °C sample for cycles 0–9.

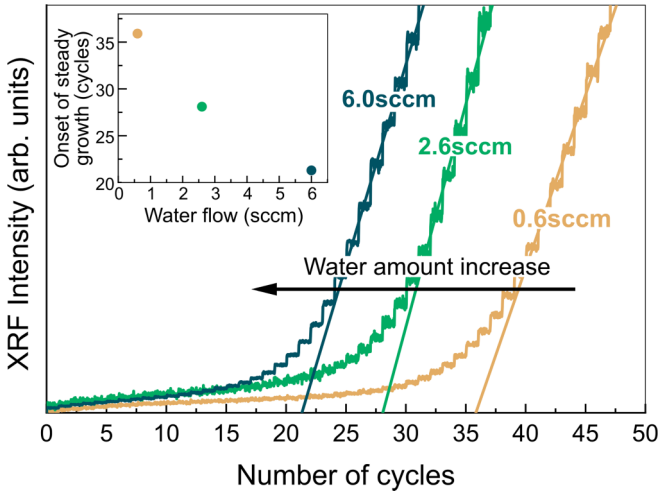

FIG. 2. XRF curves measured continuously during *in situ* ALD at the same substrate temperature of 120°C and for different water flows during the oxidant pulse: 0.6, 2.6, and 6.0 sccm. The straight line cross point with the cycle number axis gives a representative value of the onset of the steady-state growth. The value is reported in the inset as a function of water flow.

for the growth of ZnO on ZnO [29,30], and the fluorescence intensity was measured during the nitrogen purge at the end of every two cycles. For the 240 °C sample, the intensity was monitored throughout the growth process—even during the precursor/oxidant chemical reactions.

After the growth of each sample (i.e., after 100 ALD cycles), the final thickness and roughness of the ZnO layer were determined by XRR; cross-sectional TEM images were used for measuring the thicknesses, too (see Fig. S1 in the supplemental material [31]). The thickness value obtained for 100 cycles was then used to scale and calibrate the fluorescence intensity [denoted hereafter as Thickness(XRF)]. Although such a calibration would give the true thickness if the ZnO layer density remained constant during growth, this is likely not the case before the steady growth is reached. Three different regimes of growth can be distinguished, as seen in Fig. 1: the transient regime (regimes I and II), which includes an initial, slow linear growth (regime I), followed by nonlinear growth (regime II), and steady, linear growth (regime III).

The growth per cycle (GPC) calculated in growth regime III is equal to 0.17 nm cy^{-1} for the three lowest temperatures: 120, 160, and 200 °C. The equivalent thickness curve [Thickness(XRF)] for the highest substrate temperature of 240 °C shows the same general trend. However, a higher growth rate is observed in regime I, and the GPC value in regime III is larger (0.22 nm cy^{-1}). Note that the initial growth rate (corresponding to the slope during the three first cycles) is higher than the one observed for the following cycles in growth regime I (inset of Fig. 1).

Some ALD parameters can strongly influence the nucleation process. We studied the impact of water coverage, measuring the XRF intensity during the entire ALD process for three different water flows, i.e., for three different water pressures (the reactor chamber was closed during the water pulse). For a 40 s injection pulse and water flow equal to 0.6, 2.6, and 6.0 sccm, the water pressure increase in the reactor chamber was 0.07, 0.32, and 0.69 mbar, respectively. The substrate temperature was 120 °C. Figure 2 shows that the XRF intensity starts to increase approximately after 21, 28, and 36 cycles for water flows of 6.0, 2.6, and 0.6 sccm, respectively. The higher the amount of water, the larger the number of water molecules that react with the sample surface, and the earlier the occurrence of the steady-state regime.

B. ZnO crystallization during growth

Reciprocal space maps were measured after different cycle numbers for three substrate temperatures: 120, 160, and 200 °C. During the RSM measurements, the samples were kept under a constant 100 sccm flow of nitrogen. By performing on-the-fly scanning of the sample (zap-scans), each RSM map could be acquired in approximately 15 min. We employ the BINOCULARS data reduction software [28] to plot the RSMs. Figure 3 shows a set of RSMs measured at a substrate temperature of 200 °C, with the reciprocal-lattice units (r.l.u.) referenced to the InGaAs cubic lattice parameter $a = 0.586\,87$ nm.

To better observe the intensity dynamics of the ZnO diffraction peaks (or rings, as in the case of powder diffraction), the 220 InGaAs peak was subtracted from all RSM images. This was performed by selecting a background image containing the InGaAs Bragg peak and subtracting it from all subsequent images. For example, the RSM measured at 36 ALD cycles was chosen as the background image for sample 200, since ZnO diffraction peaks (rings) were absent for cycle 36. The results show that during growth, in-plane ZnO diffraction rings gradually appear, and their intensities increase with the ALD cycle number. To identify the ZnO reflections, we measured the radii of the diffraction rings, which are inversely proportional to the interplanar distances, and we referenced the distances to the ICDD database for ZnO wurtzite (PDF: 00-036-1451). In ascending radii, the three

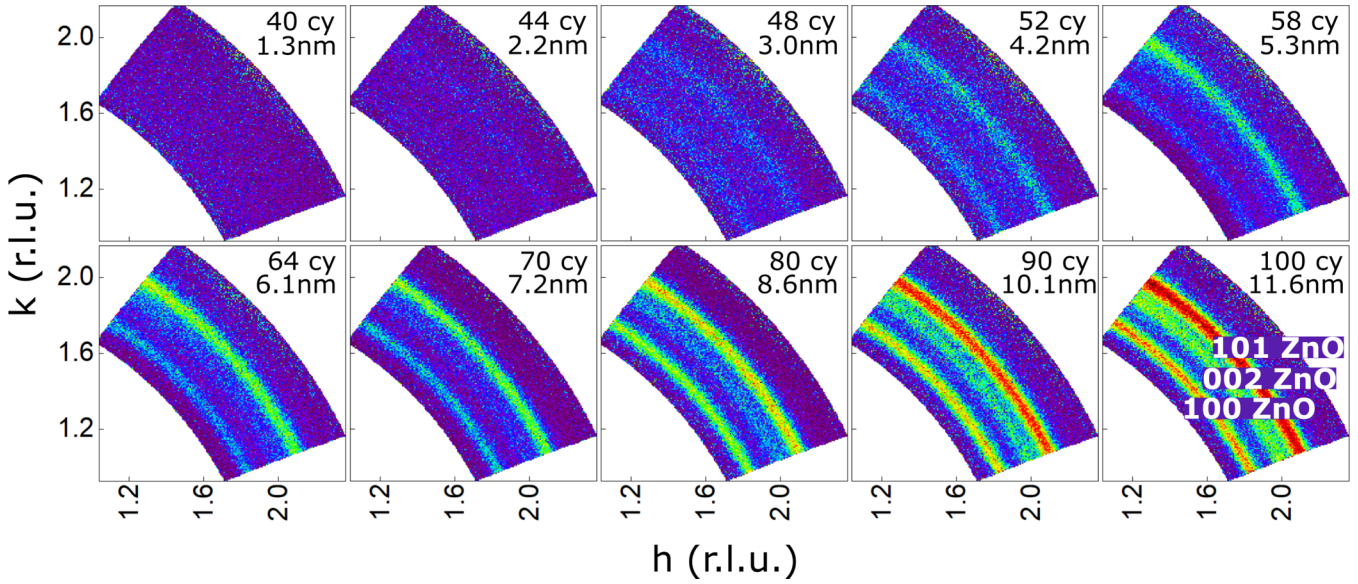

FIG. 3. Reciprocal space maps (RSMs) or fast zap-scans measured at the end of ALD cycle number 40, 44, 48, 52, 58, 64, 70, 80, 90, and 100 (the cycle numbers are shown in the figures) for a substrate temperature of 200 °C. The RSM images are plotted in InGaAs reciprocal-lattice units (r.l.u.). The images are background-subtracted.

observable diffraction rings correspond to the **100**, **002**, and **101** ZnO diffraction peaks.

Similar RSM measurements were carried out for samples 120, 160, and 200. For sample 240, only one RSM image was measured at the end of the growth (100 ALD cycles). We note that the uniform intensity along the diffraction rings indicates the absence of in-plane texture for all samples. This was also observed for the ALD growth of ZnO on SiO_2 [25]. Here, no epitaxial relationship was expected since the SiO_2 was amorphous.

Given that synchrotron radiation can readily detect crystallinity from small volumes [21,27] and that we exploit the grazing incidence geometry to probe a large area of the sample and minimize the substrate signal, the initial absence of in-plane peaks is most likely explained by the synthesis of an amorphous ZnO layer on the InGaAs substrate, which then acts as a seed layer for nucleation of the wurtzite phase. To analyze the intensity variation of the weak diffraction peaks (rings) as a function of ALD cycle number, we integrated the intensity values over the azimuthal angle (i.e., over the available arc of intensity for a fixed ring radius) and extracted the intensity profile as a function of the inverse q-vector. Figure 4 shows the intensity versus q^{-1} profile for substrate temperatures of 120, 160, 200, and 240 °C at the end of growth (100 cycles).

As already reported in the case of ZnO ALD, (001)-fiber texture develops whenever the growth temperature or the thickness is increased (see, for instance, Boichot *et al.* [25] and references therein). To look for the appearance of (001)-fiber texture for ZnO grains as a function of growth temperature, we normalized the diffraction curves with respect to the intensity of the **100** peak. The larger the number of grains that have the (001) planes parallel to the growth surface, the larger (or smaller) the **100** (versus **002**) intensity (in-plane diffraction). The **101** Bragg peak is from another family of grains. Also, the larger the number of grains that have the (001) planes parallel to the growth surface, the larger the **100** (versus **101**) intensity.

Figure 4 shows that when increasing the substrate temperature from 120 to 240 °C, the **002** and **101** diffraction intensities decrease with respect to the **100** reflection. At 240 °C, which corresponds to a temperature outside of the ALD window, the decrease of the **002** and **101** diffraction peak intensities (with respect to the **100** peak) is much more pronounced than at the lower temperatures. This relative intensity change shows that the ZnO/InGaAs film develops (001)-fiber texture at higher temperatures, as was observed for ALD-grown ZnO/*a*-SiO_2 thin films [25]. The final film thickness for sample 240 (16 nm) is also larger than the ones grown at lower substrate temperatures (12 nm), as shown in Fig. 1.

To determine the dynamics of ZnO crystallization during growth, the three diffraction peaks were fitted using Pearson VII functions; the background was subtracted beforehand.

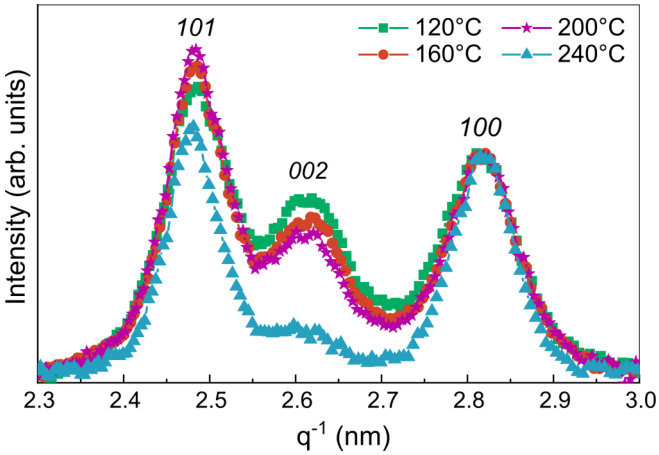

FIG. 4. The azimuth-integrated intensity profile obtained from in-plane zap-scan images as a function of $q^{-1} = (\frac{2\sin\theta}{\lambda})^{-1}$ for samples 120, 160, 200, and 240, measured after 100 ALD cycles. For comparison of the relative peak heights, all curves were normalized with respect to the intensity of the **100** diffraction peak.

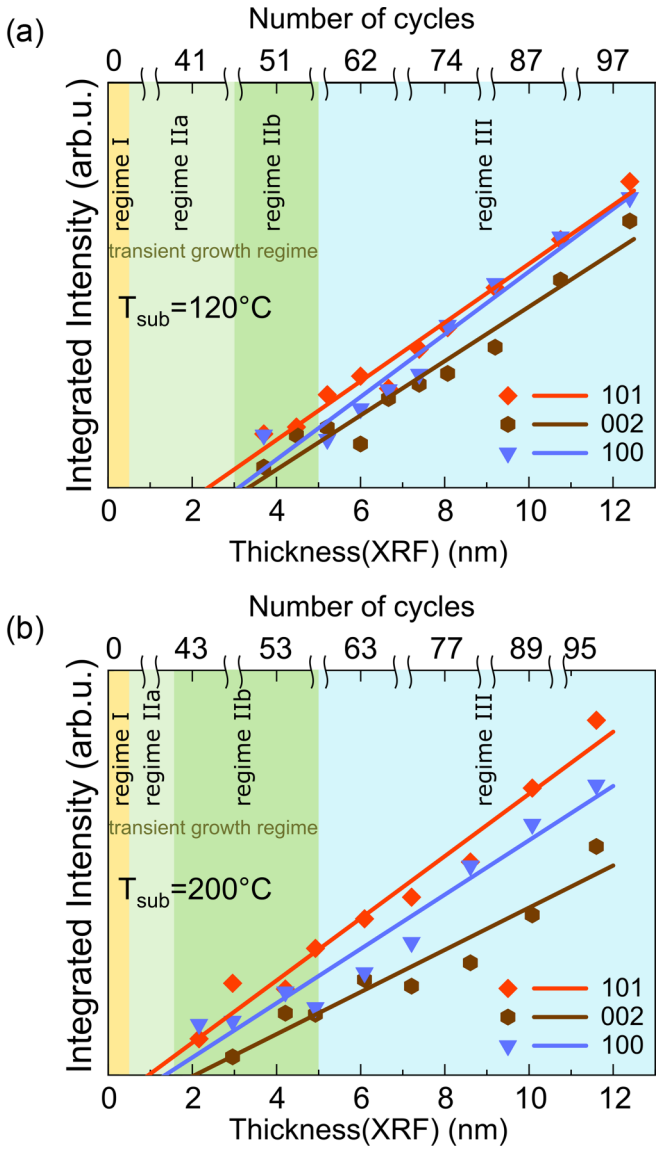

FIG. 5. The integrated **100**, **002**, and **101** diffraction peak intensities (symbols) as a function of the ZnO layer thickness (bottom x-axis) and cycle number (top x-axis) for samples grown at (a) 120 °C and (b) 200 °C. Also shown are linear fits to the data.

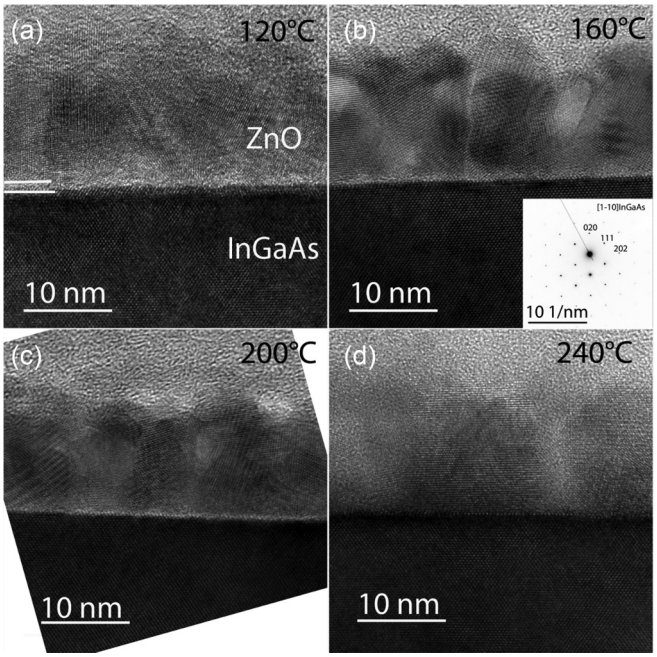

FIG. 6. Cross-sectional TEM images of samples grown at 120 °C (a), 160 °C (b), 200 °C (c), and 240 °C (d) after 100 ALD cycles. The inset in (b) shows the InGaAs diffraction plane perpendicular to the [1$\bar{1}$0] zone axis.

The intensity values for each of the three profiles were then integrated. The integrated intensities as a function of ALD cycle number for samples grown at 120 and 200 °C are shown in Figs. 5(a) and 5(b), respectively. The x-axis of Fig. 5 corresponds to the equivalent thickness (nm) on the bottom, which corresponds to Thickness(XRF) in Fig. 1, and the cycle number (in some nonlinear scale) on top.

We see in Fig. 5(a) that at a temperature of 120 °C, the integrated intensities for all three diffraction peaks are close to zero for small film thickness values (0–3 nm). This means that atomic long-range order either does not exist or the proportion of crystallinity is too small to be detected. The solid lines in Fig. 5(a) represent fits to the **101**, **002**, and **001** integrated intensities. The intersections of the lines with zero intensity give the minimum thickness for observable crystallinity, i.e., about 2–4 nm at 120 °C, and 1–2 nm at 200 °C. It is interesting to follow how the peak intensities vary with the different growth regimes indicated in Fig. 1. The different background colors in Fig. 5 indicate the different growth regimes: regime I (yellow), regime II (green), and regime III (blue). According to our previous ZnO/InGaAs x-ray absorption near-edge structure (XANES) study [26], a poorly ordered material appears after the first few growth cycles (regime I). At the beginning of 3D growth (regime IIa), the XANES spectra show the emergence of a wurtzitelike crystal structure; however, the diffraction intensity remains absent. Long-range order appears in regime IIb, as the ZnO grain size becomes large enough to result in a detectable diffraction peak. The peak intensities continue to rise, and the GPC becomes constant in regime III.

Figures 6(a)–6(d) show TEM images obtained after 100 ALD cycles for all of the samples. At 120 °C, an amorphous layer of material can be observed at the interface between the crystalline InGaAs substrate and ZnO grains. As seen in Figs. 6(b) and 6(c), increasing the growth temperature improves the crystallinity, and the amount of amorphous material at the interface decreases. At 200 °C, one can observe that the amorphous layer thickness is drastically reduced. The TEM images obtained for the sample grown at 240 °C show a thicker ZnO layer, approximately 16.5 nm, in agreement with XRR results (see Fig. S1 in the supplemental material), and the interface remains sharp, although the presence of some amorphous material cannot be excluded. However, the interface does not look the same as that for 200 °C. This may have to do with the different growth behavior observed at 240 °C by XRF (Fig. 1). The crystallinity of ZnO grains is evidenced by the presence of sharp reflections in the electron diffraction pattern (see Fig. S2 in the supplemental material). Furthermore, the **002** reflection in the diffraction pattern is

more intense. The inverse fast Fourier transform (FFT) of the **002** reflection (Fig. S2) shows that the dominant growth orientation of ZnO grains is along the [001] direction, in agreement with fiber texture discussed above.

IV. DISCUSSION

A. ZnO ALD on InGaAs, transient regime

The x-ray data presented above were obtained *in situ* during the growth of ZnO on InGaAs. When compared to the existing literature, whether *ab initio* calculations or Monte Carlo simulations, they provide new insight, particularly with regard to the transient growth regime that often exists but with properties that depend on the growth parameters. This insight enables the construction of a simple growth model that we present in Sec. IV D. Here we describe a few prominent and systematic experimental observations in the transient regime.

In agreement with our previous findings [26], the transient growth regime is comprised of two different growth modes corresponding to regimes I and II in Fig. 1. The transient growth regime I (growth delay) is characterized by a significant jump of the deposition rate at cycle 1 (see the inset of Fig. 1 and Ref. [26]), and then by a relatively low GPC (on the order of few hundredths of a nm cy^{-1}), which is linear and concomitant with Zn desorption, as observed by Zn x-ray fluorescence measurements [26]. We believe this is most likely due to DEZn precursor desorption: the chemisorbed DEZn remains on the surface whereas the physisorbed DEZn molecules are removed during the purging process. At a growth temperature equal to 120 °C, we observed that regime I ends with the cessation of DEZn desorption and the formation of a poorly ordered, ultrathin ZnO layer [26]. As the GPC starts to increase, growth enters regime II.

The transient growth regime II is characterized by a nonlinear (S-shaped) [32] thickness-versus-cycle curve, similar to the one observed in the case of type II substrate-inhibited growth in Ref. [32]. More precisely, the GPC increases as the square of the cycle number reaches a maximum, and then decreases to a constant value. This type of growth behavior is associated with 3D island growth. In the present case, we associate regime II with the nucleation and growth of ZnO grains (3D) on top of the poorly ordered Zn oxide layer (2D) synthesized during regime I. The formation of ZnO grains increases the surface roughness; as a consequence, both the surface area and growth rate increase. As the surface begins to smooth, the growth rate is reduced. The transient growth regime II ends when the GPC reaches a constant level, thereby entering regime III.

The regime I growth behavior reported here and previously [26,33] is very similar to that of HfO_2 ALD on SiO_2 on silicon. Dkhissi *et al.* [34] showed by density functional theory (DFT) calculations and kinetic Monte Carlo (kMC) simulations that the jump in growth rate during the first ALD cycle is the result of the metal precursor reaction with OH groups already present on the SiO_2/Si substrate surface. The degree of surface hydroxylation is determined by the substrate temperature and the chemical and physical preparation process [35]. Due to the consumption of most of the OH groups during the first cycle and slow surface hydrolysis, they then observed a low growth rate until the coverage reached 100%. According to the authors, the rate of transition to a thin, continuous oxide film depends on the degree of surface hydrolysis during the water pulses, with the development of ionic structure occurring through densification. This accounts for the transition from molecular groups to the crystalline material and leads to an increase of the metal and oxygen coordination numbers [34,36,37].

Weckman *et al.* [38,39] performed extensive *ab initio* calculations on ZnO ALD on ZnO from DEZn and H_2O. They showed that in addition to the standard ligand exchange reactions for DEZn, hydroxyl groups, monoethyl zinc (MEZn), and water molecules, many other processes, including densification, can occur during the precursor and oxidant reactions, eventually leading to crystalline ZnO. Gao *et al.* [30] gave experimental evidence of a reaction between grafted molecular ligands and the surface, as well as reactions between two grafted molecules in standing positions. Most generally, during ZnO ALD on ZnO, the Zn metallic precursor adsorbs to a surface oxygen site (e.g., water, hydroxyl group, or oxygen) and reacts with a proton of a neighboring hydroxyl group to form MEZn and release an ethane molecule. Densification increases the coordination numbers of Zn and O atoms and can occur prior to ligand exchange: i.e., Zn molecular groups (or O molecular groups) move from the oxygen sublattice (Zn sublattice) of the target ZnO wurtzite structure to the nearest-neighbor vacant site of the metal (oxygen) sublattice.

In the present study, hydrolysis of the InGaAs surface is not as efficient as hydrolysis of the ZnO surface; this leads to a growth delay (regime I in Fig. 1). Since the GPC behavior and surface coverage in the growth regime I are similar to those observed during HfO_2 ALD on SiO_2, it is reasonable to propose that the growth in regime I proceeds predominantly via densification mechanisms. By the end of regime I, at the atomic scale, the crystallographic structure can be described as embryonic wurtzite (according to XAFS spectroscopy) [26]. This experimental finding corroborates the existence of densification mechanisms in the very early stages of ZnO ALD on InGaAs.

As noted above, the amount of water flow, i.e., the water pressure in the present case, impacts the growth delay (Fig. 2), playing an important role in these mechanisms. We discuss this point further below.

B. Water pressure on transient regime I

We showed in Fig. 2 that the water flow has a strong effect on the duration of regime I. We presume that increasing the water flow leads to an increase of OH-group density on the growth surface, curtailing the growth delay [40–43]. It is known that the oxidant flow can influence the initial stages of ALD by modifying the surface density of hydroxyl groups. For instance, Matero *et al.* [44] found that by increasing the water pulse time and flow, the growth rate initially increases before reaching a constant. They attributed this to an increase of hydroxyl group density on the surface after the water pulse. For substrate temperatures higher than 450 °C, the growth rate was found to decrease, partly due to decomposition of the surface hydroxyl groups [45]. Sweet and Parsons [46] performed *in situ* conductance measurements

during ZnO ALD on polypropylene, nylon-6, SiO_2, TiO_2, and Al_2O_3 substrates for growth temperatures between 100 and 175 °C. They showed that physisorbed water contributes to conduction, and that when water desorbs, the net conductance decreases. For most of the substrates a growth delay was observed, and the conductance measurement showed water desorption during the delay. The authors suggested that the nucleation rate depends on the density of reactive hydroxyl sites on the growth surface.

In the present case, one can hypothesize that during the water pulse, the coverage of new OH groups on the InGaAs surface increases for higher water pressures inside the reactor chamber. This could lead to an increase in the number of DEZn molecules chemisorbed or adsorbed on the InGaAs surface and a shorter growth delay. However, this assumption currently lacks theoretical support, and DFT calculations or Monte Carlo simulations are beyond the scope of the present study. We do find that a long water pulse prior to the first ALD cycle does not change the growth delay. According to *ab initio* calculations performed by Weckman *et al.* for the case of ZnO ALD on ZnO [38,39], water molecules adsorb to Zn atoms on the growth surface, with an amount dependent on the number of accessible oxygen sites near the bare Zn or MEZn sites. Interestingly, the authors showed that the adsorption energy for a water molecule on the Zn atom of MEZn is −0.4 eV, while the adsorption energy for an adjacent second water molecule is −0.27 eV. However, the additional water molecule decreases the ligand exchange activation energy from 1.15 to 0.91 eV. Therefore, an increase of the water pressure inside the reactor chamber can increase the number of chemisorbed water molecules (and thus the water molecule cooperative effects); this, in turn, could lead to the adsorption of more DEZn molecules during the next DEZn pulse and favor ligand exchange and densification. Such effects could help to explain why the growth delay is curtailed when increasing the water pressure inside the reactor chamber (Fig. 2). We note that the substrate temperature in the ALD window [13,47], unlike the water flow, does not affect the initial growth mode.

C. Substrate temperature effect on ZnO growth

In Sec. III B we reported that the substrate temperature is a parameter strongly affecting the texture and crystallization of the growing ZnO layer. In-plane surface diffraction shows no in-plane texture for any of the substrate temperatures used in our experiments. However, an increase in the substrate temperature leads to the development of out-of-plane (001)-fiber texture (see Fig. 4); the effect is especially pronounced for sample 240. The appearance of (001)-fiber texture was already reported for ZnO ALD on Si. When the deposition temperature is above 220 °C, the [001] growth direction is preferred [15,25,48].

The substrate temperature also affects the initial crystallization behavior. In agreement with a previous study [26], Fig. 5(a) and the postgrowth TEM image in Fig. 6(a) show that a poorly ordered oxide layer forms on the InGaAs substrate at 120 °C prior to the growth of crystalline ZnO. By increasing the substrate temperature to 200 °C, it is clear from Fig. 5(b) that for an equivalent layer thickness, the proportion of crystalline material is larger than that for 120 °C. In addition, the postgrowth TEM image in Fig. 6(c) shows that the thickness/amount of poorly ordered materials has decreased. The ZnO layer adjacent to the InGaAs is almost fully crystalline. (Note that the total thicknesses for samples 120 and 200 are nearly the same). Similar crystalline transitions have already been reported for oxide ALD. Unlike our study, however, the results were obtained by postgrowth characterization. Libera *et al.* [49] found that ZnO ALD on silica gel under similar conditions begins with an amorphous layer prior to crystallization. Aarik *et al.* [50] showed that the growth of ZrO_2 films on silicon and silica starts with the formation of an amorphous layer. An increase of deposition temperature from 180 to 600 °C leads to a decrease of ZrO_2 amorphous layer thickness from 50 to 5 nm. Similar results were also reported for HfO_2 films grown on silica and silicon by ALD [51,52].

In the regime of steady growth, we observe that the GPC obtained at 240 °C (0.22 nm cy^{-1}) is higher than the GPC value obtained for the three other substrate temperatures inside the ALD window (0.17 nm cy^{-1}). At high temperatures, outside of the ALD window, the thermal energy can be high enough to decompose the precursors (pyrolysis) and start additional reactions on the sample surface [13,47]. However, according to *ab initio* calculations [53], the activation energy value for the pyrolysis of DEZn (or MEZn) is rather high (on the order of 2 eV or more), which precludes the reaction during ALD. Another possible mechanism that could explain the increase in GPC at high temperature stems from the results of *ab initio* calculations by Weckman *et al.* [38,53]. After a first ligand-exchange reaction between adsorbed DEZn and surface hydroxyl groups, a second slow reaction of MEZn to bare zinc atoms becomes possible. The later reaction leads to an increase of the GPC by increasing the amount of adsorbed DEZn (steric repulsion between Zn precursors is lowered) and the appearance of bare Zn sites for water molecules to adsorb to during the water pulse. This second reaction has an activation energy in the range of 0.92–1.52 eV, which is higher than the initial ligand-exchange reaction between the adsorbed DEZn and surface hydroxyl groups and is more likely at higher temperatures. Finally, regarding the initial growth, we note that the growth delay is about the same for samples 120, 160, 200, and 240, unlike the effect of water flow. The reason for this remains uncertain, and further investigations are necessary.

D. Growth model of ZnO ALD on InGaAs

During the ALD process, the nature of the metal precursor or oxidant reaction with the surface depends strongly on the surface chemistry and functionalization [54]. In the present study, we showed that the early stages of ZnO growth on InGaAs are quite different from ZnO steady growth on ZnO. In Fig. 7, we summarize and schematize the initial growth of ZnO on atomically flat InGaAs.

In regime I, the metal precursor (DEZn) and oxidant (H_2O) chemisorb at random positions to the substrate surface, and surface reactions produce grafted molecules that cover gradually the substrate surface and undergo a densification mechanism. Meanwhile, barely any growth has occurred in

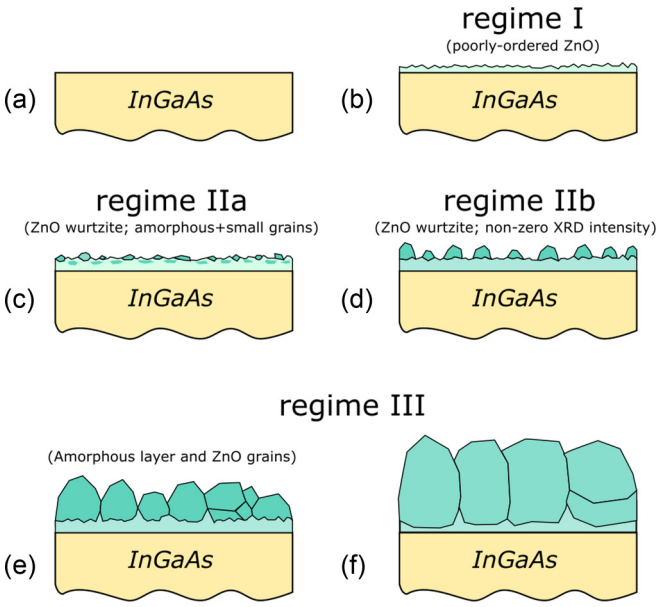

FIG. 7. Model for ZnO growth on InGaAs for the 120-200 °C substrate temperature range. We depict cross-sections for (a) the InGaAs substrate; (b) the sample in regime I, with poorly ordered ZnO structure; (c) the sample after formation of the initial, wurtzite-like structure (regime IIa); (d) the sample after ZnO growth with long-range order (regime IIb); (e) the sample after reaching steady growth and larger ZnO grains (regime III); and (f) the sample after steady growth with a probable crystallization of amorphous ZnO (regime III).

the direction normal to the substrate [Fig. 7(b)]. By the end of regime I, the InGaAs substrate surface is covered with an ultrathin, poorly ordered Zn oxide layer [Fig. 7(c)]. When entering regime II, the growth rate and surface roughness increase due to 3D growth and the formation of grains. The transition from regime I to II is clearly evidenced with the appearance on the XAFS spectra of the characteristic features of the wurtzite structure (see Fig. S3 and the results of a previous study [26,55,56]). In regime II, the thickness curve versus cycle number (Fig. 1) is reminiscent of substrate-inhibited growth of type II [32], exhibiting the signature S-shape. After nucleation of the crystallization centers, the ZnO grains grow, and the surface roughness increases up to a maximum before decreasing after coalescence. Concomitantly, the growth rate increases nonlinearly up to a maximum prior to decreasing and becoming constant after grain coalescence [26]. This behavior was initially described by a model proposed by Nilsen *et al.* [57,58] for simulating polycrystalline growth. According to in-plane x-ray diffraction (Fig. 5), none of the films show long-range order at the start of regime II [regime IIa in Fig. 7(c)]. Diffraction peaks are detected only when the in-plane size and the amount of crystalline material are large enough, as in regime IIb [Fig. 7(d)]. The minimum thickness required for the transition from regime IIa to IIb is lower when increasing the substrate (growth) temperature. To explain layer crystallization during ALD, Hausmann and Gordon [59] proposed a growth model for HfO_2 and ZrO_2 ALD on silicon. The authors hypothesize that the growth of crystalline grains starts from a nucleus that appears at random on the surface of the amorphous layer. During the next ALD cycles, the crystallites grow in size, both in the direction perpendicular and parallel to the substrate surface, and new crystallization centers form. The crystallites eventually coalesce to yield a uniform crystalline layer. When the probability of a crystallization event is low, a poorly ordered layer is created. The authors showed that higher deposition temperatures increase the number of nucleation events, leading to improved film crystallinity. Our experimental results generally agree with this model. Incidentally, based on the postgrowth TEM image [Fig. 6(d)] as well as on the diffraction intensity versus thickness trend [Figs. 5(a) and 5(b)], it can be assumed that for sample 240 there is no evidence of growth in regime IIa. However, this issue remains open and deserves further *in situ* XRD and XAFS investigations during growth. Then, for all of the studied samples, growth eventually enters the steady regime, i.e., the growth rate becomes constant [regime III, Figs. 7(e) and 7(f)].

V. CONCLUSIONS

In summary, we conducted detailed investigations into the growth of ZnO on InGaAs by atomic layer deposition, which allowed the construction of a cycle-dependent growth model, as seen in Fig. 7. While in the ALD window, growth takes place in different regimes depending on the total film thickness. Consequently, the results may be critical to those utilizing ultrathin ZnO layers for device applications. We find that both *in situ* techniques during deposition and a variety of different synchrotron x-ray methods are essential for understanding the ALD process, especially at the earliest stages.

ACKNOWLEDGMENTS

This work has been partially supported by the LabEx Minos ANR-10-LABX-55-01 funded by the "Investments for the Future" Program. Financial support for this work by ANR projects ANR-11-NANO-0014 and ANR-15-IDEX-02 is gratefully acknowledged. D.D.F. was supported by both an award from the Nanosciences Foundation and the U.S. Department of Energy, Office of Science, Office of Basic Energy Sciences, Materials Sciences and Engineering Division. We acknowledge D. De Barros for the engineering assistance. We thank the European Synchrotron Radiation Facility (ESRF) for beamtime allocation (proposal number 82779) and facilities placed at our disposal at beamline ID3, and in particular T. Dufrane, H. Isern, and H. Lopez for their help with the experimental setup.

[1] M. Heyns and W. Tsai, MRS Bull. **34**, 485 (2009).
[2] J. A. Del Alamo, Nature (London) **479**, 317 (2011).
[3] J. C. Woolley, M. B. Thomas, and A. G. Thompson, Can. J. Phys. **46**, 157 (1968).

[4] J. W. Wagner, J. Electrochem. Soc. **117**, 1193 (1970).

[5] S. Oktyabrsky and D. Y. Peide, *Fundamentals of III-V Semiconductor MOSFETs* (Springer, New York 2010).

[6] A. Agrawal, N. Shukla, K. Ahmed, and S. Datta, Appl. Phys. Lett. **101**, 042108 (2012).

[7] D. Connelly, C. Faulkner, D. Grupp, and J. Harris, IEEE Trans. Nanotechnol. **3**, 98 (2004).

[8] J. Robertson, J. Vac. Sci. Technol. A **31**, 050821 (2013).

[9] C.-Y. Chang, O. Ichikawa, T. Osada, M. Hata, H. Yamada, M. Takenaka, and S. Takagi, J. Appl. Phys. **118**, 085309 (2015).

[10] S. H. Kim, S. Y. Joo, H. S. Jin, W.-B. Kim, and T. J. Park, ACS Appl. Mater. Interfaces **8**, 20880 (2016).

[11] L. Chen, Z. Yu-Ming, Z. Yi-Men, and L. Hong-Liang, Chin. Phys. B **22**, 076701 (2013).

[12] M.-H. Liao and C. Lien, AIP Adv. **5**, 057117 (2015).

[13] S. M. George, Chem. Rev. **110**, 111 (2009).

[14] A. Pakkala and M. Putkonen, in *Handbook of Deposition Technologies for Films and Coatings* (Elsevier, Amsterdam, 2010), pp. 364–391.

[15] T. Tynell and M. Karppinen, Semicond. Sci. Technol. **29**, 043001 (2014).

[16] V. Miikkulainen, M. Leskelä, M. Ritala, and R. L. Puurunen, J. Appl. Phys. **113**, 2 (2013).

[17] D. Fong, J. Eastman, S. Kim, T. Fister, M. Highland, P. Baldo, and P. Fuoss, Appl. Phys. Lett. **97**, 191904 (2010).

[18] Z. Baji, Z. Lábadi, Z. E. Horváth, G. Molnár, J. Volk, I. Bársony, and P. Barna, Cryst. Growth Des. **12**, 5615 (2012).

[19] K. Knapas and M. Ritala, Crit. Rev. Solid State Mater. Sci. **38**, 167 (2013).

[20] F. Zaera, Coord. Chem. Rev. **257**, 3177 (2013).

[21] K. Devloo-Casier, K. F. Ludwig, C. Detavernier, and J. Dendooven, J. Vac. Sci. Technol. A **32**, 010801 (2014).

[22] J. A. Klug, M. S. Weimer, J. D. Emery, A. Yanguas-Gil, S. Seifert, C. M. Schlepütz, A. B. Martinson, J. W. Elam, A. S. Hock, and T. Proslier, Rev. Sci. Instrum. **86**, 113901 (2015).

[23] J. Dendooven, E. Solano, M. M. Minjauw, K. Van de Kerckhove, A. Coati, E. Fonda, G. Portale, Y. Garreau, and C. Detavernier, Rev. Sci. Instrum. **87**, 113905 (2016).

[24] E. Skopin, Ph.D. thesis, Grenoble Alpes, 2018.

[25] R. Boichot, L. Tian, M.-I. Richard, A. Crisci, A. Chaker, V. Cantelli, S. Coindeau, S. Lay, T. Ouled, C. Guichet, M. H. Chu, N. Aubert, G. Ciatto, E. Blanquet, O. Thomas, J.-L. Deschanvres, D. D. Fong, and H. Renevier, Chem. Mater. **28**, 592 (2016).

[26] E. V. Skopin, L. Rapenne, H. Roussel, J.-L. Deschanvres, E. Blanquet, G. Ciatto, D. D. Fong, M.-I. Richard, and H. Renevier, Nanoscale **10**, 11585 (2018).

[27] O. Balmes, R. van Rijn, D. Wermeille, A. Resta, L. Petit, H. Isern, T. Dufrane, and R. Felici, Catal. Today **145**, 220 (2009).

[28] S. Roobol, W. Onderwaater, J. Drnec, R. Felici, and J. Frenken, J. Appl. Crystallogr. **48**, 1324 (2015).

[29] E. B. Yousfi, J. Fouache, and D. Lincot, Appl. Surf. Sci. **153**, 223 (2000).

[30] Z. Gao, F. Wu, Y. Myung, R. Fei, R. Kanjolia, L. Yang, and P. Banerjee, J. Vac. Sci. Technol. A **34**, 01A143 (2016).

[31] See Supplemental Material at http://link.aps.org/supplemental/10.1103/PhysRevMaterials.4.043403 for complementary x-ray reflectivity curves, transmission electron microscopy images and Zn K-edge, *in situ* X-ray Absorption Near Edge Structure Spectra.

[32] R. L. Puurunen and W. Vandervorst, J. Appl. Phys. **96**, 7686 (2004).

[33] E. V. Skopin, J.-L. Deschanvres, and H. Renevier, Phys. Status Solidi A 1900831 (2020).

[34] A. Dkhissi, G. Mazaleyrat, A. Estève, and M. D. Rouhani, Phys. Chem. Chem. Phys. **11**, 3701 (2009).

[35] L. Zhuravlev, Colloids Surf., A **173**, 1 (2000).

[36] S. Olivier, J.-M. Ducéré, C. Mastail, G. Landa, A. Estève, and M. D. Rouhani, Chem. Mater. **20**, 1555 (2008).

[37] C. Mastail, C. Lanthony, S. Olivier, J.-M. Ducéré, G. Landa, A. Estève, M. D. Rouhani, N. Richard, and A. Dkhissi, Thin Solid Films **520**, 4559 (2012).

[38] T. Weckman and K. Laasonen, J. Phys. Chem. C **122**, 7685 (2018).

[39] T. Weckman, M. Shirazi, S. D. Elliott, and K. Laasonen, J. Phys. Chem. C **122**, 27044 (2018).

[40] M. Alam and M. Green, J. Appl. Phys. **94**, 3403 (2003).

[41] R. L. Puurunen, Appl. Surf. Sci. **245**, 6 (2005).

[42] K. Tapily, D. Gu, and H. Baumgart, ECS Trans. **33**, 355 (2010).

[43] M. L. Green, M.-Y. Ho, B. Busch, G. D. Wilk, T. Sorsch, T. Conard, B. Brijs, W. Vandervorst, P. I. Räisänen, D. Muller, M. Bude, and J. Grazul, J. Appl. Phys. **92**, 7168 (2002).

[44] R. Matero, A. Rahtu, M. Ritala, M. Leskelä, and T. Sajavaara, Thin Solid Films **368**, 1 (2000).

[45] A. Ott, J. Klaus, J. Johnson, and S. George, Thin Solid Films **292**, 135 (1997).

[46] W. J. Sweet III and G. N. Parsons, Langmuir **31**, 7274 (2015).

[47] J. Ferguson, A. Weimer, and S. George, J. Vac. Sci. Technol. A **23**, 118 (2005).

[48] S.-Y. Pung, K.-L. Choy, X. Hou, and C. Shan, Nanotechnology **19**, 435609 (2008).

[49] J. Libera, J. Elam, and M. Pellin, Thin Solid Films **516**, 6158 (2008).

[50] J. Aarik, A. Aidla, H. Mändar, T. Uustare, and V. Sammelselg, Thin Solid Films **408**, 97 (2002).

[51] J. Aarik, A. Aidla, H. Mändar, V. Sammelselg, and T. Uustare, J. Cryst. Growth **220**, 105 (2000).

[52] J. Aarik, A. Aidla, A.-A. Kiisler, T. Uustare, and V. Sammelselg, Thin Solid Films **340**, 110 (1999).

[53] T. Weckman and K. Laasonen, J. Phys. Chem. C **120**, 21460 (2016).

[54] J.-W. Lim, H.-S. Park, and S.-W. Kang, J. Electrochem. Soc. **148**, C403 (2001).

[55] M. H. Chu, L. Tian, A. Chaker, V. Cantelli, T. Ouled, R. Boichot, A. Crisci, S. Lay, M.-I. Richard, O. Thomas, J.-L. Deschanvres, H. Renevier, D. D. Fong, and G. Ciatto, Cryst. Growth Des. **16**, 5339 (2016).

[56] M.-H. Chu, L. Tian, A. Chaker, E. Skopin, V. Cantelli, T. Ouled, R. Boichot, A. Crisci, S. Lay, M.-I. Richard *et al.*, J. Electron. Mater. **46**, 3512 (2017).

[57] O. Nilsen, O. B. Karlsen, A. Kjekshus, and H. Fjellvåg, Thin Solid Films **515**, 4538 (2007).

[58] O. Nilsen, O. B. Karlsen, A. Kjekshus, and H. Fjellvåg, Thin Solid Films **515**, 4550 (2007).

[59] D. M. Hausmann and R. G. Gordon, J. Cryst. Growth **249**, 251 (2003).